Dynamical electron vortices in attosecond double photoionization of H_2

J. M. Ngoko Djiokap,[1] A. V. Meremianin,[2] N. L. Manakov,[2] L. B. Madsen,[3] S. X. Hu,[4] and Anthony F. Starace[1]

[1]*Department of Physics and Astronomy, University of Nebraska, Lincoln, Nebraska 68588-0299, USA*

[2]*Department of Physics, Voronezh State University, Voronezh 394006, Russia*

[3]*Department of Physics and Astronomy, Aarhus University, DK-8000 Aarhus C, Denmark*

[4]*Laboratory for Laser Energetics, University of Rochester, Rochester, New York 14623-1299, USA*

(Received 13 June 2018; published 7 December 2018)

We study electron momentum vortices in single-photon double ionization of H_2 by time-delayed, counter-rotating, elliptically polarized attosecond pulses propagating along $\hat{\mathbf{k}}$ either parallel or perpendicular to the molecular axis $\mathbf{R}$. For $\hat{\mathbf{k}} \parallel \mathbf{R}$, *kinematical* vortices occur similar to those found for He. For $\hat{\mathbf{k}} \perp \mathbf{R}$, we find *dynamical* vortex structures originating from an ellipticity-dependent interplay of $^1\Sigma_u^+$ and $^1\Pi_u^+$ continuum amplitudes. We propose a complete experiment to determine the magnitudes and relative phase of these amplitudes by varying pulse ellipticities and time delays.

DOI: 10.1103/PhysRevA.98.063407

I. INTRODUCTION

An unusual kind of Ramsey interference [1] was recently predicted to result in matter-wave vortex structures in the electron momentum distributions resulting from single ionization of He by a pair of time-delayed, counter-rotating, circularly polarized attosecond pulses [2]. The vortex structures and electron angular distributions were shown to be exquisitely sensitive to the pulse polarizations and their time delay. These sensitivities indicate applications to both laser pulse diagnostics and control of electron motions. Electron momentum vortices for multiphoton single ionization of He were also predicted [3]. These predictions were confirmed experimentally for three-photon [4] and four-photon [5] single ionization of potassium atoms using time-delayed, circularly polarized femtosecond pulses. The predictions of electron vortices in single ionization of He [2,3] also stimulated a number of theoretical studies of the occurrence of electron vortices in other systems and processes, including in ionization of single-electron molecular ions [6,7], in single-photon [8] and multiphoton [9] double ionization of He, in pair production processes [10], and in H-atom strong-field ionization processes [11–13].

Although Refs. [2] and [3] treated two-electron correlations in *single* photoionization processes, perturbation theory (PT) analyses showed that vortices produced by single-color fields originate from kinematic factors that are independent of the photoionization dynamics. Similarly, for *double* photoionization (DPI) of He (in which electron correlation is essential) by time-delayed, oppositely elliptically polarized attosecond pulses it was shown that such *kinematical* vortices occur for a particular class of electron detection geometries in which one can extract a dynamically independent kinematic factor from the sixfold differential probability (SDP) [8]. The occurrence of *dynamical* vortices (in which dynamical amplitudes depend on the azimuthal angles of the photoelectrons) was not observed in single-color DPI of He [8]. However, the nonspherical symmetry of the H_2 molecule offers the possibility of uncovering features that do not occur for spherically symmetric atomic targets, such as the occurrence of heretofore unexpected *dynamical* vortices.

In this paper we study occurrence of vortices in electron momentum distributions produced in single-photon ($\hbar\omega = 75$ eV) double ionization of fixed-in-space H_2 in its $^1\Sigma_g^+$ ground state by time-delayed, counter-rotating, elliptically polarized (chiral) attosecond pulses for two cases: $\hat{\mathbf{k}} \parallel \mathbf{R}$ and $\hat{\mathbf{k}} \perp \mathbf{R}$, where $\hat{\mathbf{k}}$ is the laser propagation direction and $\mathbf{R}$ is the internuclear axis. Our results are based on *ab initio* numerical solutions of the six-dimensional time-dependent Schrödinger equation (TDSE) and analytic PT analyses. We report five main findings: (i) For $\hat{\mathbf{k}} \parallel \mathbf{R}$, only $^1\Pi_u^+$ continuum states are excited and *kinematical* vortices occur under the same conditions as in DPI of He [8]. (ii) For $\hat{\mathbf{k}} \perp \mathbf{R}$, both $^1\Sigma_u^+$ and $^1\Pi_u^+$ continuum states are excited by each pulse and unexpected *dynamical* vortices are found to originate from Ramsey interference of the two resulting electron wave packets. (iii) The occurrence of the dynamical vortices can be controlled by the pulse ellipticities. (iv) For fixed excess energy E, the time delay τ between pulses allows control of the A_Σ and A_Π amplitude contributions to the two-electron angular distributions. (v) Combining these features, *we propose a complete experiment* in which both the magnitudes and the relative phase of the A_Σ and A_Π amplitudes can be determined by varying the pulse ellipticities and time delays.

This paper is organized as follows. In Sec. II we provide a brief description of our numerical methods. In Sec. III we present our analytical and numerical results for DPI of H_2 by time-delayed, counter-rotating, elliptically polarized attosecond pulses propagating along $\hat{\mathbf{k}}$ either parallel or perpendicular to the molecular axis $\mathbf{R}$. For each of these two cases, we present results for the momentum distributions of the two ionized electrons. We then focus on the $\hat{\mathbf{k}} \perp \mathbf{R}$ case, presenting the two-electron angular distributions and proposing a complete experiment for determining the magnitudes and relative phases of the two dynamical amplitudes involved in this DPI process. In Sec. IV we summarize our key results

and present our conclusions. Finally, in Appendix A we give results of various tests we have carried out to confirm the convergence of our numerical results, and in Appendix B we present analytical PT derivations of the key equations used to interpret our numerical results. Atomic units (a.u.) are used throughout this paper unless specified otherwise.

II. BRIEF DESCRIPTION OF NUMERICAL METHODS

In this section we begin by providing a brief overview of *ab initio* computational methods that have been used to study DPI of the H_2 molecule. We then briefly describe the methods we have used in this work.

Ab initio numerical calculations of the triply differential cross sections (TDCS) for DPI of H_2 have been carried out using two different representations of the two-electron wave functions. One group of calculations used a single-center spherical coordinate representation [14–17], while a second group of calculations used a two-center prolate spheroidal coordinate representation [18–20]. The first calculations for the TDCS were done in spherical coordinates using either the time-independent exterior complex scaling (ECS) method [16,17] or the time-dependent close-coupling (TDCC) method [14]. Taking into account the experimental uncertainties in the scattering angles, the agreement between the theoretical calculations and experimental results was good [14,16,17]. Subsequently, three calculations were carried out in prolate spheroidal coordinates, using the ECS method [18] and the TDSE method [19,20]. Also, another TDSE calculation was carried out in spherical coordinates using a single-center partial-wave expansion of the wave packet in terms of bipolar harmonics [15]. For a laser pulse linearly polarized either along or perpendicular to the molecular axis, the TDCS results obtained by these different methods were compared in Refs. [15,19,20]. Except for the TDCS obtained within the ECS method in prolate spheroidal coordinates [18], excellent agreement was found between the prolate spheroidal coordinate results [19,20] and those in spherical coordinates using the ECS method [17], the TDCC method with a larger box size than in [14] (see Refs. [15,19]), and a variant of the TDSE method [15].

To obtain the SDP for DPI of H_2 numerically, we have generalized our code for solving the two-electron TDSE for He interacting with chiral (i.e., elliptically-polarized) pulses [2,3,8,21] to take into account the two-center H_2 problem within the fixed-nuclei approximation (as in Refs. [14–20]). As in Refs. [14] and [15], we use a single-center, time-dependent close-coupling expansion [14,15] of the two-electron wave packet in spherical coordinates (with the origin at the center of mass of the nuclei). To discretize the radial part of the two-electron wave packet, we use a finite-element discrete variable representation (FE-DVR) [22] in which 60 finite elements equally spaced by 2 a.u. are used. An eight-point Gauss-Legendre-Lobatto basis is used within each FE, which yields a total of 421 DVR functions in each radial coordinate up to 120 a.u. [23]. To efficiently time propagate the wave packet $\Psi(\mathbf{r}_1, \mathbf{r}_2; R, t)$ for chiral pulses, we employ a real-space-product algorithm [23] together with a Wigner rotation transformation [24,25]. After the end of the pair of time-delayed laser pulses with total duration $T_f = \tau + T$ (where T is the total duration of each pulse and τ is the time delay between the two laser pulses), we freely propagate in time the wave packet $\Psi(\mathbf{r}_1, \mathbf{r}_2; R, t)$ (i.e., the solution of the TDSE) for a longer additional time T_p in order to ensure that its doubly ionized part, $\Psi_C(\mathbf{r}_1, \mathbf{r}_2; R, T_f + T_p)$, is sufficiently far away from the nuclei, and also so that the two photoelectrons are well separated from each other [15,19]. At a time $t = T_f + T_p$ (where $T_p = 13$–20 optical cycles), we obtain the SDP as

$$\mathcal{W} = \left|\left\langle \Psi^{(-)}_{\mathbf{p}_1,\mathbf{p}_2}(\mathbf{r}_1, \mathbf{r}_2)\middle|\Psi_C(\mathbf{r}_1, \mathbf{r}_2; R, T_f + T_p)\right\rangle\right|^2. \quad (1)$$

Here Ψ_C equals the two-electron wave packet (that we obtain by solving the TDSE within a radial box of 120 a.u.) from which we have removed contributions of bound and singly ionized states (as done in Refs. [15,26]). The field-free double-continuum final state $\Psi^{(-)}_{\mathbf{p}_1,\mathbf{p}_2}$ with excess energy E is approximated by a product of two Coulomb waves with charge $Z = 2$ [15,19]. All our TDSE results have been verified to be converged (see Appendix A).

III. ANALYTICAL AND NUMERICAL RESULTS

For H_2 in its $^1\Sigma_g^+$ ground state (with binding energy $E_b \simeq 51.4$ eV) interacting with two pulses, each having a carrier frequency $\omega = 75$ eV and an intensity of 5×10^{13} W/cm^2, first-order PT is valid. For right or left circularly polarized pulses, with $\hat{\mathbf{k}} \parallel \mathbf{R}$, only transitions $^1\Sigma_g^+ \rightarrow {}^1\Pi_u^+$, with $\Delta M = +1$ or -1, respectively, are allowed by electric dipole selection rules in LS coupling for this (linear in intensity) DPI process. For elliptically polarized light with $\hat{\mathbf{k}}$ not parallel to $\mathbf{R}$ (e.g., $\hat{\mathbf{k}} \perp \mathbf{R}$), $\Delta M = 0, \pm1$ transitions $^1\Sigma_g^+ \rightarrow (^1\Sigma_u^+, {}^1\Pi_u^+)$ are allowed. The first-order PT amplitude for DPI of the $^1\Sigma_g^+$ ground state of H_2 by *two* chiral pulses can be written in a form similar to that for a single pulse [27]:

$$\begin{aligned}\mathcal{A} = e^{-i\phi_1}\{&A_{\Pi,1}(\chi)(\mathbf{e}'\cdot\hat{\mathbf{p}}_1) + A_{\Pi,2}(\chi)(\mathbf{e}'\cdot\hat{\mathbf{p}}_2)\\ &+(\hat{\mathbf{R}}\cdot\mathbf{e}')[A_{\Sigma,1}(\chi) - A_{\Pi,1}(\chi)](\hat{\mathbf{R}}\cdot\hat{\mathbf{p}}_1)\\ &+(\hat{\mathbf{R}}\cdot\mathbf{e}')[A_{\Sigma,2}(\chi) - A_{\Pi,2}(\chi)](\hat{\mathbf{R}}\cdot\hat{\mathbf{p}}_2)\},\end{aligned} \quad (2)$$

where the coefficients $A_{\Pi,i}$ and $A_{\Sigma,i}$, $i = 1, 2$, are true scalar functions of χ,

$$\chi \equiv (p_1, p_2, R, u, u_1, u_2), \quad (3)$$

where p_1, p_2 are the magnitudes of the electron momenta, $R = 1.4$ a.u. is the internuclear separation, $u \equiv (\hat{\mathbf{p}}_1\cdot\hat{\mathbf{p}}_2)$ and $u_{1,2} \equiv (\hat{\mathbf{R}}\cdot\hat{\mathbf{p}}_{1,2})$. The coefficients $A_{\Pi,i}$ and $A_{\Sigma,i}$ depend upon parameters of the pair of pulses other than their effective polarization vector $\mathbf{e}' = \mathbf{e}_1 + e^{i\Phi}\mathbf{e}_2$ (see Ref. [8]), where $\mathbf{e}_j = (\hat{\boldsymbol{\epsilon}} + i\eta_j\hat{\boldsymbol{\zeta}})/(1+\eta_j^2)^{1/2}$ is the polarization vector of the jth pulse, with $-1 \leqslant \eta_j \leqslant +1$ being its ellipticity, and $\hat{\boldsymbol{\epsilon}}$ and $\hat{\boldsymbol{\zeta}} = (\hat{\mathbf{k}}\times\hat{\boldsymbol{\epsilon}})$ being respectively the major and minor axes of the polarization ellipse. The relative phase $\Phi = (E + E_b)\tau + \phi_{12}$ in the effective polarization vector $\mathbf{e}'$ has two terms: $(E + E_b)\tau$, the phase accumulated by the first created electronic wave packet when the second pulse delayed in time by τ strikes the system in its initial quantum state, and $\phi_{12} \equiv \phi_1 - \phi_2$, the relative carrier-envelope phase (CEP) between the two pulses.

The amplitude (2) holds for *any orientation* of the vectors $\mathbf{p}_1(\theta_1, \varphi_1)$, $\mathbf{p}_2(\theta_2, \varphi_2)$, and $\mathbf{R}$. Our PT analysis and

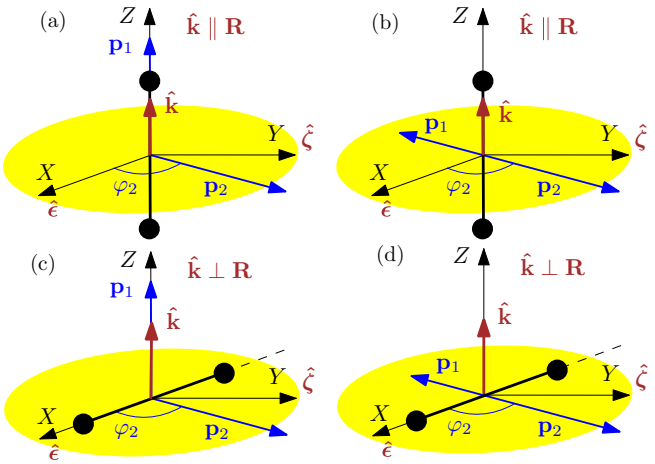

FIG. 1. Electron detection geometries for DPI of H_2 by a pair of time-delayed oppositely elliptically-polarized pulses propagating parallel ($\hat{\mathbf{k}} \parallel \mathbf{R}$, top) or perpendicular ($\hat{\mathbf{k}} \perp \mathbf{R}$, bottom) to the internuclear vector $\mathbf{R}$, with $\hat{\mathbf{k}}$ the laser propagation direction. Left column: $\mathbf{p}_1 \parallel \hat{\mathbf{k}}$ and $\mathbf{p}_2$ is in the laser polarization plane $(\hat{\boldsymbol{\epsilon}}, \hat{\boldsymbol{\zeta}})$ with spherical angles $(\theta_2 = \pi/2, \varphi_2)$, with $\mathbf{p}_1$ and $\mathbf{p}_2$ denoting the momenta of the outgoing electrons. Right column: back-to-back emission of electrons in the polarization plane where $\theta_1 = \theta_2 = \pi/2$ and $\varphi_2 = \varphi_1 - \pi$. In all panels, $0 \leqslant \varphi_2 \leqslant 2\pi$ and we fix $\hat{\mathbf{k}} \parallel \hat{\mathbf{z}}$, $\hat{\boldsymbol{\epsilon}} \parallel \hat{\mathbf{x}}$, and $\hat{\boldsymbol{\zeta}} \parallel \hat{\mathbf{y}}$. The origin of coordinates is at the center of mass of the nuclei.

numerical TDSE results below are for counter-rotating pulses ($\eta \equiv \eta_1 = -\eta_2$) and two-electron detection geometries [in which $u \equiv (\hat{\mathbf{p}}_1 \cdot \hat{\mathbf{p}}_2)$ is fixed] for each of two light propagation directions (see Fig. 1): (i) $\hat{\mathbf{k}} \parallel \mathbf{R}$, and (ii) $\hat{\mathbf{k}} \perp \mathbf{R}$. For *both* cases, the amplitude (2) can be rewritten as a superposition of two kinematic vortex factors, $\cos(\Phi/2 \pm \hat{\xi}\varphi_2)$, having opposite handedness (see Appendix B):

$$\mathcal{A} = A_\eta^{(+)} \cos(\Phi/2 - \hat{\xi}\varphi_2) + A_\eta^{(-)} \cos(\Phi/2 + \hat{\xi}\varphi_2), \quad (4)$$

where $\mathbf{p}_2$ is in the polarization plane ($\theta_2 = \pi/2$), the dynamical amplitudes $A_\eta^{(\pm)}$ depend on χ, and $\hat{\xi} \equiv \xi/|\xi|$, with $\xi = 2\eta/(1+\eta^2)$ being the circular polarization degree. Note that $\xi = +1$ or -1 corresponds to right-left or left-right circularly polarized (RLCP or LRCP) pulses.

A. Kinematical vortices in the $\hat{\mathbf{k}} \parallel \mathbf{R}$ geometry

In the $\hat{\mathbf{k}} \parallel \mathbf{R}$ geometry [see Figs. 1(a) and 1(b)], the dynamical amplitudes in Eq. (4) for $\mathcal{A} \equiv \mathcal{A}_\parallel$ take the form (see Appendix B),

$$A_{\eta,\parallel}^{(\pm)} = e^{i(\Phi/2-\phi_1)}\sqrt{(1+\ell)/2}(1 \pm |\eta|)A_\Pi(\chi), \quad (5)$$

$$= e^{i(\Phi/2-\phi_1)}\sqrt{(1 \pm |\xi|)}A_\Pi(\chi), \quad (6)$$

where $\ell = (1-\eta^2)/(1+\eta^2)$ is the linear polarization degree, $A_\Pi(\chi) \equiv A_{\Pi,2}(\chi)$ for the detection geometry in Fig. 1(a), and $A_\Pi(\chi) \equiv A_{\Pi,2}(\chi) - A_{\Pi,1}(\chi)$ for that in Fig. 1(b). For circularly polarized pulses, $|\eta| = 1$ so that $A_{\pm1,\parallel}^{(-)} = 0$. Consequently, the SDP $\mathcal{W}_\parallel = |\mathcal{A}_\parallel|^2$ becomes

$$\mathcal{W}_\parallel(\mathbf{p}_2) = 2|A_\Pi(\chi)|^2 \cos^2(\Phi/2 - \xi\varphi_2), \quad (7)$$

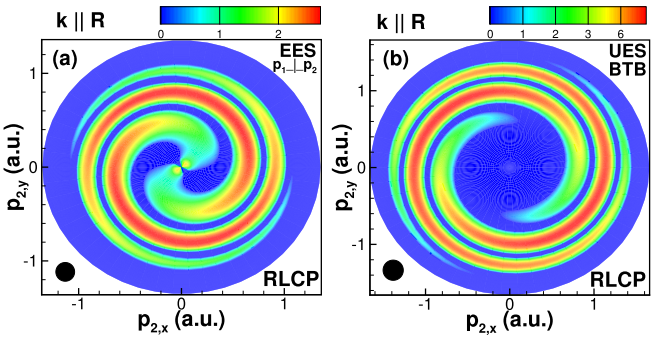

FIG. 2. Momentum $\mathbf{p}_2$ distributions in the polarization plane for DPI of fixed-in-space H_2 by right-left circularly polarized (RLCP) attosecond pulses with $\hat{\mathbf{k}} \parallel \mathbf{R}$ (indicated by a single black dot) delayed in time by $\tau = T \simeq 331$ as. (a) SDP(10^{-8} a.u.) for the detection geometry in Fig. 1(a) and equal energy sharing (EES); (b) SDP(10^{-7} a.u.) for the BTB geometry in Fig. 1(b) and unequal energy sharing (UES) of degree $\varepsilon = E_1/E = 25\%$, where $5.6 \leqslant E \leqslant 41.6$ eV. Each pulse has carrier frequency $\omega = 75$ eV, zero CEP, intensity $I = 5\times10^{13}$ W/cm^2, $n = 6$ cycles, total duration $T \simeq 331$ as, a $\cos^2$ temporal profile, and bandwidth $\Delta\omega \simeq 1.44\omega/n = 18$ eV.

which has exactly the same form as in both single [2] and double [8] photoionization of the He $^1S^e$ ground state. The dynamical coefficient $|A_\Pi(\chi)|^2$ in (7) (as for those in Refs. [2,8]) has no angular dependence, since u, u_1, and u_2 in χ [see Eq. (3)] are fixed for both detection geometries. Thus, the maxima and zeros of the kinematical factor $\cos^2(\Phi/2 - \xi\varphi_2)$ define Fermat (or Archimedean) spirals [2]. The spiral equations are $\varphi_2^{\max}(E) = \xi\Phi/2 + n\pi$ for maxima and $\varphi_2^{\text{zero}}(E) = \xi\Phi/2 + (n+1/2)\pi$ for zeros, where $n = 0, \pm1, \pm2, \ldots$ give the number of spiral arms, which is 2 since only $n = 0, 1$ give independent equations. Thus, the $\mathbf{p}_2$ distribution in the polarization xy plane ($\theta_2 = \pi/2$) produced by time-delayed RLCP or LRCP pulses exhibits atomlike two-arm oppositely handed spiral *kinematical vortices*, i.e., *counterclockwise* for RLCP and *clockwise* for LRCP. Our TDSE results for the $\mathbf{p}_2$ distributions produced by time-delayed RLCP pulses (with parameters specified in the caption of Fig. 2) are shown in Fig. 2(a) for equal energy sharing (EES) in the detection geometry of Fig. 1(a), and in Fig. 2(b) for back-to-back (BTB) electron emission in the polarization xy plane [Fig. 1(b)] with an unequal-energy-sharing (UES) partition of $\varepsilon = E_1/E = 25\%$. Our TDSE results confirm well all vortex features predicted by PT.

B. Dynamical vortices in the $\hat{\mathbf{k}} \perp \mathbf{R}$ geometry

In the $\hat{\mathbf{k}} \perp \mathbf{R}$ geometry [see Figs. 1(c) and 1(d)], the dynamical amplitudes in Eq. (4) for $\mathcal{A} \equiv \mathcal{A}_\perp$ take the form (see Appendix B)

$$A_{\eta,\perp}^{(\pm)}(\chi) = e^{i(\Phi/2-\phi_1)}\sqrt{(1+\ell)/2}[A_\Sigma(\chi) \pm |\eta|A_\Pi(\chi)], \quad (8)$$

where $A_\Pi(\chi) \equiv A_{\Pi,2}(\chi)$, $A_\Sigma(\chi) \equiv A_{\Sigma,2}(\chi)$, with $\chi = (p_1, p_2, R, 0, 0, \cos\varphi_2)$ for the geometry in Fig. 1(c), and $A_\Pi(\chi) \equiv A_{\Pi,2}(\chi) - A_{\Pi,1}(\chi)$, $A_\Sigma(\chi) \equiv A_{\Sigma,2}(\chi) - A_{\Sigma,1}(\chi)$, with $\chi = (p_1, p_2, R, -1, -\cos\varphi_2, \cos\varphi_2)$ for that in Fig. 1(d). Note that since both amplitudes, $A_\Pi(\chi)$ and $A_\Sigma(\chi)$, in Eq. (8) depend on the azimuthal angle φ_2 of $\mathbf{p}_2$ via

χ, spiral vortex structures are unexpected. Indeed, the SDP $\mathcal{W}_\perp \equiv |\mathcal{A}_\perp|^2$ takes the form (see Appendix B)

$$\begin{aligned}\mathcal{W}_\perp(\mathbf{p}_2) &= 2(1-\ell)|A_\Pi(\chi)|^2 \sin^2\varphi_2 \sin^2(\Phi/2) \\ &+ 2(1+\ell)\,|A_\Sigma(\chi)|^2 \cos^2\varphi_2 \cos^2(\Phi/2) \\ &+ \xi\,\mathrm{Re}\,[A_\Sigma^*(\chi)A_\Pi(\chi)]\sin(2\varphi_2)\sin\Phi, \qquad (9)\end{aligned}$$

which does not obviously have vortex structure. However, if A_Π were equal to A_Σ, then the SDP in (9) reduces for circular polarization ($\ell = 0$, $\xi = \pm 1$) to the same form as in (7) with its kinematic vortex factor. Thus, Eq. (9) *may* produce vortex structures in particular cases. The analysis is best done for the general amplitude in Eq. (4) using the dynamical amplitudes in Eq. (8).

The DPI amplitudes for the $\hat{\mathbf{k}} \parallel \mathbf{R}$ and $\hat{\mathbf{k}} \perp \mathbf{R}$ geometries have the same form (4), i.e., a superposition of two kinematic vortex factors $\cos(\Phi/2 \pm \hat{\xi}\varphi_2)$ with opposite handedness, so that the occurrence of vortices requires one of the amplitudes in (4) to be larger than the other. Also, the φ_2 dependence of the dynamical amplitudes must be "weaker" than that of the kinematic factors $\cos(\Phi/2 \pm \hat{\xi}\varphi_2)$. For $\hat{\mathbf{k}} \parallel \mathbf{R}$, the $A_\Pi(\chi)$ amplitude in Eq. (5) has no angular dependence and the occurrence of vortices is determined by the amplitude ratio, $A^{(-)}_{\eta,\parallel}/A^{(+)}_{\eta,\parallel} = (1-|\eta|)/(1+|\eta|)$, which depends only on the ellipticity η. In contrast, for $\hat{\mathbf{k}} \perp \mathbf{R}$ the occurrence of vortices is controlled by the amplitude ratio $A^{(-)}_{\eta,\perp}/A^{(+)}_{\eta,\perp} = (A_\Sigma - |\eta|A_\Pi)/(A_\Sigma + |\eta|A_\Pi)$, which depends not only on the ellipticity η, but also on the magnitudes and relative phase of the $A_\Pi(\chi)$ and $A_\Sigma(\chi)$ amplitudes, both of which depend on the azimuthal angle φ_2 of $\mathbf{p}_2$. (Note that for $\omega \simeq 75$ eV the magnitude of A_Π can be as much as a factor of 5 larger than that of A_Σ [28–30].) If the SDP in (9) leads to vortex structures, these are *dynamical vortices* rather than kinematical vortices since their occurrence depends on the interplay between the participating dynamical amplitudes, $A_\Pi(\chi)$ and $A_\Sigma(\chi)$. For the two $\hat{\mathbf{k}} \perp \mathbf{R}$ geometries in Figs. 1(c) and 1(d), our TDSE results in Figs. 3(a), 3(b) and 3(d) do show dynamical vortex structures, while there are none in Fig. 3(c).

For the geometry in Fig. 1(c), TDSE results for the $\mathbf{p}_2$ distributions by RLCP pulses delayed in time by $\tau = T \simeq 331$ as are shown in Fig. 3(a) for EES and in Fig. 3(b) for an UES ($\varepsilon = 25\%$). The $\mathbf{p}_2$ distributions exhibit vortex structures for any energy-sharing partition. These dynamical vortex patterns differ from the kinematical ones shown for $\hat{\mathbf{k}} \parallel \mathbf{R}$ in Figs. 2(a) and 2(b). First, they are distorted owing to the angular dependences and the relative magnitudes of the A_Σ and A_Π amplitudes. Second, they have an opposite handedness, since the $A^{(-)}_{\eta,\perp}$ term in (4) dominates, i.e., $A_\Sigma \approx -A_\Pi$ [cf. Eq. (8)]. For LRCP pulses, the handedness changes. For RLCP pulses, the ratio Υ of the energy- and angle-integrated A_Π amplitude to that of the A_Σ amplitude is ≈ 2 for both EES and UES in this geometry. We find dynamical vortices in this geometry occur for $0.15 \leqslant |\eta| \leqslant 1$ and are best seen for $\eta \approx 0.5$, as confirmed by our TDSE results.

For the BTB detection geometry [Fig. 1(d)] with an UES partition of $\varepsilon = 25\%$, $\Upsilon \sim 8$ for RLCP pulses ($|\eta| = 1$). As $A_\Pi \gg A_\Sigma$, Eq. (8) shows that $A^{(\pm)}_{\eta,\perp} \approx \pm A_\Pi$. Thus the

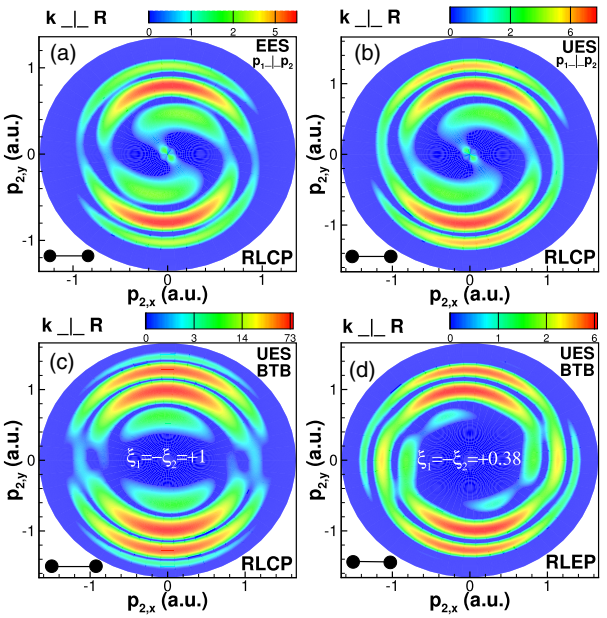

FIG. 3. Momentum $\mathbf{p}_2$ distributions in the polarization plane for DPI of fixed-in-space H_2 by right-left chiral attosecond pulses with $\hat{\mathbf{k}} \perp \mathbf{R}$ (indicated by the dumbbell shape) delayed in time by $\tau = 331$ as. Top row: SDP(10^{-8} a.u.) by RLCP pulses for the detection geometry in Fig. 1(c) for (a) EES and (b) UES with $\varepsilon = 25\%$. Bottom row: SDP(10^{-8} a.u.) for the BTB geometry in Fig. 1(d) for an UES ($\varepsilon = 25\%$) produced by (c) RLCP pulses and (d) right-left elliptically polarized (RLEP) pulses with $\xi \equiv \xi_1 = -\xi_2 = +0.38$.

counter-rotating vortices in (4) overlap,

$$\begin{aligned}\mathcal{A} &\simeq A_\Pi(\chi)[\cos(\Phi/2 - \hat{\xi}\varphi_2) - \cos(\Phi/2 + \hat{\xi}\varphi_2)], \\ &= A_\Pi(\chi)\sin(\hat{\xi}\varphi_2)\sin(\Phi/2), \qquad (10)\end{aligned}$$

producing a dipolar pattern along the y axis with Ramsey fringes [see Fig. 3(c)]. The same pattern is obtained (not shown) when using LRCP pulses. This absence of vortex patterns in Fig. 3(c) can also be well understood by only retaining the first term (with $\ell = 0$ for RLCP or LRCP pulses) of the SDP (9), since the second and third terms in (9) can be dropped when $\Upsilon \sim 8$ (i.e., $A_\Sigma \ll A_\Pi$).

By tuning the ellipticity η over the range $0.05 \leqslant |\eta| \leqslant 0.5$, however, spiral vortices similar to those in the $\hat{\mathbf{k}} \parallel \mathbf{R}$ geometry become visible, as shown in Fig. 3(d) for $\eta = +0.2$ (or $\xi = 0.38$). To visualize the dependence of this electron phenomenon on η, we provide in the Supplemental Material [31] an animation showing the evolution with the ellipticity η (over the broader range $0.001 \leqslant |\eta| \leqslant 1$) of the dynamical vortex patterns for the BTB detection geometry [Fig. 1(d)] and the same laser parameters as in Fig. 3(c). Although $A_\Pi \gg A_\Sigma$, the vortex structures appear for η in the range $0.05 \leqslant |\eta| \leqslant 0.5$, because $|\eta|A_\Pi$ becomes comparable to A_Σ. Consequently, depending on the relative phase of the A_Σ and A_Π amplitudes, one expects either $A^{(+)}_{\eta,\perp} \propto [A_\Sigma(\chi) + |\eta|A_\Pi(\chi)]$ or $A^{(-)}_{\eta,\perp} \propto [A_\Sigma(\chi) - |\eta|A_\Pi(\chi)]$ to dominate. In Fig. 3(d) for the BTB detection geometry [Fig. 1(d)] and RLCP pulses, the *counterclockwise* handedness of the vortices implies

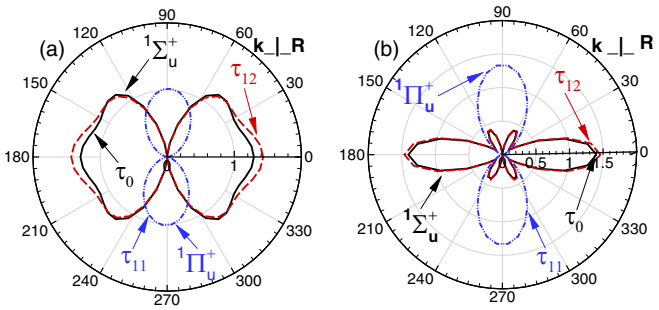

FIG. 4. Time-delay sensitivity of the angular distributions (in units of 10^{-8} a.u.) for the faster electron with momentum $\mathbf{p}_2$ at a fixed excess energy $E = \omega - E_b = 23.6$ eV and for an UES ($\varepsilon = E_1/E = 25\%$) scheme produced by RLCP attosecond pulses with $\mathbf{k} \perp \mathbf{R}$. (a) Results for the detection geometry in Fig. 1(c); (b) results for the detection geometry in Fig. 1(d). The relative CEP is $\phi_{12} = 0$ and results are given for three time delays: τ_0, τ_{11}, and τ_{12}, where $\tau_n = n\pi/\omega$. Results for τ_{11} are scaled by 1/10 and 1/64 respectively in (a) and (b).

$A^{(+)}_{\eta,\perp} \gg A^{(-)}_{\eta,\perp}$, so that

$$\mathcal{W}_\perp \equiv |A_\perp|^2 \approx |A^{(+)}_{\eta,\perp}(\chi)|^2 \cos^2(\Phi/2 - \hat{\xi}\varphi_2), \tag{11}$$

where $\hat{\xi} \equiv \xi/|\xi|$. In Figs. 3(a) and 3(b) for the orthogonal detection geometry [Fig. 1(c)] and RLCP pulses, the *clockwise* handedness of the vortices implies $A^{(-)}_{\eta,\perp} \gg A^{(+)}_{\eta,\perp}$, so that

$$\mathcal{W}_\perp \equiv |A_\perp|^2 \approx |A^{(-)}_{\eta,\perp}(\chi)|^2 \cos^2(\Phi/2 + \hat{\xi}\varphi_2). \tag{12}$$

It is thus clear that for both $\hat{\mathbf{k}} \perp \mathbf{R}$ geometries, the spiral handedness depends not only on the sign of ξ but also on the relative phase of the A_Σ and A_Π amplitudes. Alternatively, the third term ($\propto \xi\,\mathrm{Re}\,[A^*_\Sigma(\chi)A_\Pi(\chi)]$) in (9) shows this also, where χ differs for the two detection geometries, as specified below Eq. (8).

1. Time-delay periodicity of the angular distributions

For fixed energy E and $\phi_{12} = 0$, the dependence of the SDP (9) on the relative phase $\Phi = (E + E_b)\tau + \phi_{12}$ predicts a time-delay periodicity of the electron angular distributions. Specifically, for a time delay $\tau_n = n\pi/(E + E_b)$, where n is an odd integer, only the A_Π amplitude contributes to the SDP, whereas if n is an even integer only the A_Σ amplitude contributes, as shown by our TDSE angular distributions for $E = 23.6$ eV in Fig. 4 for the two $\hat{\mathbf{k}} \perp \mathbf{R}$ detection geometries in Figs. 1(c) and 1(d). Note that the minor discrepancies in the TDSE results for τ_0 and τ_{12} indicate the accuracy of the PT result (9), which does not account for depletion effects.

2. Proposed complete experiment

The PT result for the SDP in Eq. (9) indicates also the possibility of doing a complete experiment in which one determines both the magnitudes and the relative phase of the A_Σ and A_Π amplitudes. Specifically, using the time-delay periodicity $\tau_n = n\pi/(E + E_b)$ of the angular distributions discussed above for even and odd integers n, one can extract the magnitudes $|A_\Sigma|$ and $|A_\Pi|$, respectively, from the first two terms of (9). As for their relative phase, the achiral first two terms on the right of (9) depend only on ℓ, so that they are invariant to whether the time-delayed, counter-rotating pulses are right-left or left-right elliptically polarized, whereas the chiral third term ($\propto \xi$) changes sign. Thus, subtraction of measurements of the SDP for right-left and left-right elliptically polarized pulses will give twice the third term in (9), which is $\propto \mathrm{Re}\,[A^*_\Sigma(\chi)A_\Pi(\chi)]$. These latter measurements should be for time delays corresponding to noninteger n, in which case the cross term ($\propto \sin\Phi$) in (9) is nonzero.

IV. SUMMARY AND CONCLUSIONS

In summary, vortices in DPI of H_2 by time-delayed counter-rotating chiral pulses are studied for two detection geometries involving fixed angular separation between electron momenta. For $\hat{\mathbf{k}} \parallel \mathbf{R}$, atomlike *kinematical* spiral vortices are predicted with a handedness given by the helicity of the first pulse. For $\hat{\mathbf{k}} \perp \mathbf{R}$, *dynamical* vortices are predicted for a wide range of ellipticities owing to the interplay of the A_Σ and A_Π dynamical amplitudes. The helicity of these vortices depends also upon the relative phase of the A_Σ and A_Π amplitudes. Finally, we have outlined a complete set of measurements allowing determination of both the magnitudes and the relative phase of these two dynamical amplitudes.

ACKNOWLEDGMENTS

The research of A.F.S. and J.M.N.D. is supported in part by the U.S. Department of Energy (DOE), Office of Science, Basic Energy Sciences, under Award No. DE-FG03-96ER14646; the research of S.X.H. is supported by the DOE National Nuclear Security Administration under Award No. DE-NA0001944, the University of Rochester, and the New York State Energy Research and Development Authority; the research of L.B.M. is supported by the VKR Center of Excellence, QUSCOPE; and the research of A.V.M. and N.L.M. is supported by the Russian Ministry of Science and Higher Education under Grants No. 3.1761.2017/4.6 and No. 3.7514.2017/8.9, respectively. Our computations used Stampede 2 at the Texas Advanced Computing Center (TACC) at the University of Texas at Austin under U.S. National Science Foundation Grant No. PHY-120003. This work was completed utilizing the Holland Computing Center of the University of Nebraska, which receives support from the Nebraska Research Initiative.

APPENDIX A: CONVERGENCE TESTS FOR DPI OF H_2 BY TIME-DELAYED CHIRAL PULSES

In this Appendix we describe three tests of the convergence of the angular distributions of the two ionized electrons with respect to their sensitivity to (1) our choice of the number of total electronic angular momenta L; (2) our choice of the projection time T_p (i.e., how long we wait after the end of our pulses before calculating the SDP); and (3) our choice of the outer radial boundary R_0 of bound and singly ionized states (which we use to remove contributions of these states from our calculated final-state wave packet).

TABLE I. Dependence of the calculated $^1\Sigma_g^+$ ground-state energy (a.u.) of the H_2 molecule for internuclear separation $R \simeq 1.4$ a.u. on the number of total electronic angular momenta L_i.

L_i	Energy (a.u.)
0	−1.784972
0,2	−1.872914
0,2,4	−1.883314
0,2,4,6	−1.888573

1. Dependence of the angular distributions on the number of total electronic angular momenta L

In contrast to the He atom, the total electronic angular momentum L is not a good quantum number for the H_2 molecule. While the spherically symmetric He atom ground state has $L = 0$, the nonspherical symmetry of the electron-nucleus interaction in the H_2 molecule Hamiltonian requires that the ground state is described using several *even* L components. In our single-center close-coupling expansion approach, we propagate the two-electron wave packet in imaginary time to obtain the energy of the $^1\Sigma_g^+$ ground state of the H_2 molecule at the equilibrium internuclear distance $R \simeq 1.4$ a.u. The dependence of the calculated H_2 ground-state energy on the number of total electronic angular momenta L_i is given in Table I. For each L_i, all combinations of individual electron orbital angular momenta $l_1, l_2 = 0 - 5$ are included. One sees that the results for two, three, and four values of L_i compare well with the benchmark values −1.888 760 a.u. [32] or −1.888 761 a.u. [33].

Starting from the ground state obtained using either $L_i = 0, 2$ or $L_i = 0, 2, 4$ angular momenta to solve the TDSE, we employ an expansion of the two-electron wave packet including either four values ($L = 0 - 3$) or five values ($L = 0 - 5$) of L, respectively. Although the total electronic angular momentum L is not a good quantum number, converged results are found using an expansion in only four values of L, $L = 0 - 3$, their azimuthal quantum numbers $|M| \leqslant L$, all combinations of individual electron orbital angular momenta $l_1, l_2 = 0 - 5$, and their azimuthal quantum numbers $|m_1| \leqslant l_1$ and $|m_2| \leqslant l_2$. Indeed, for our laser parameters, including six values of $L = 0 - 5$ (as in [15]) does not change our SDP results, as shown in Fig. 5 for two time delays $\tau = \tau_{12}$ [see Fig. 5(a)] and $\tau = \tau_{11}$ [see Fig. 5(b)], where $\tau_n = n\pi/\omega$. Here, the projection time is fixed at $T_p = 35$ a.u. and the outer radial boundary of bound and singly ionized states is fixed at $R_0 = 10$ a.u. The results shown are for the detection geometry in Fig. 1(c) for an UES scheme ($\varepsilon = E_1/E = 25\%$) at a fixed excess energy $E = \omega - E_b$.

In Fig. 5 one sees that the two-electron angular distribution is sensitive to both the time delay and the number of orbital angular momenta included in the calculation. As discussed above for the angular distribution results shown in Fig. 4, for the case $\tau = \tau_{12}$ shown in Fig. 5(a) only the $^1\Sigma_u^+$ continuum states are excited, whereas for the case $\tau = \tau_{11}$ shown in Fig. 5(b) only the $^1\Pi_u^+$ continuum states are excited. In both cases, including only total orbital angular momenta $L = 0, 1$ leads to dipolar angular distributions, either along or perpendicular to the molecular axis. However, when one includes higher values of L, the angular distribution along the molecular axis develops an additional structure, whereas that perpendicular to the molecular axis does not.

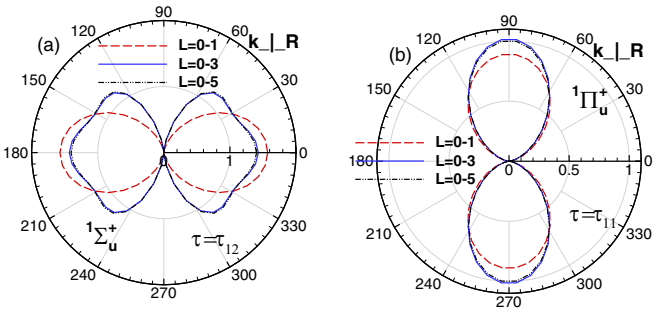

FIG. 5. Convergence of the DPI angular distributions [calculated using Eq. (1)] for the faster electron with momentum $\mathbf{p}_2$ as a function of the number of total electronic angular momenta, L, produced by RLCP attosecond pulses delayed in time by (a) $\tau = \tau_{12}$ and (b) $\tau = \tau_{11}$, where $\tau_n = n\pi/\omega$. The results are for the detection geometry in Fig. 1(c) for an UES scheme ($\varepsilon = E_1/E = 25\%$) at a fixed excess energy $E = \omega - E_b$. Plotted are results [in units of (a) 10^{-8} a.u. and (b) 10^{-7} a.u.] for $R_0 = 10$ a.u. and $T_p = 35$ a.u. for the two-electron wave packet [calculated using either four ($L = 0 - 3$) or six ($L = 0 - 5$) values of L projected onto field-free Coulomb final states with $L = 0 - 1$ [dashed (red) lines], $L = 0 - 3$ [solid (blue) lines], and $L = 0 - 5$ [dash double-dotted (black) lines]. The pulse parameters are specified in the caption of Fig. 1.

2. Dependence of the angular distributions on the projection time T_p

For the same detection scheme as in Fig. 5 [i.e., for the detection geometry in Fig. 1(c) for an UES scheme ($\varepsilon = E_1/E = 25\%$) at a fixed excess energy $E = \omega - E_b$], the

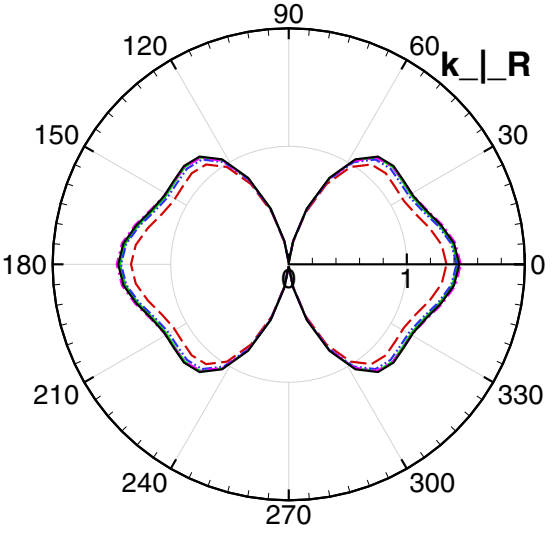

FIG. 6. Convergence of the DPI angular distributions with projection time T_p for $R_0 = 10$ a.u. and $L = 0$–3 and other parameters as in Fig. 5(a). Results [in units of 10^{-8} a.u.] are shown for five values of T_p: 20 a.u. [dashed (red) line], 25 a.u. [solid (green) line], 35 a.u. [dash double-dotted (blue) line], 40 a.u. [dash-dotted (magenta) line], and 45 a.u. [solid (black) line].

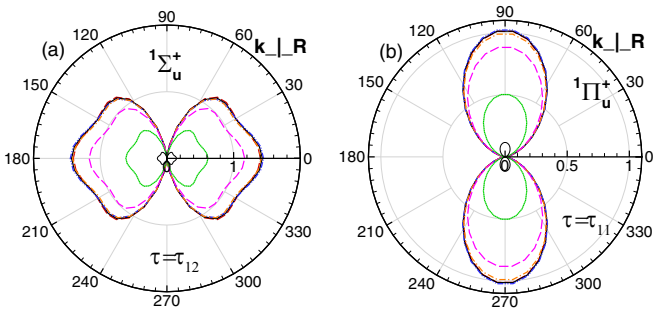

FIG. 7. Convergence of the DPI angular distributions with outer radial boundary R_0 of bound and singly ionized states for $T_p = 35$ a.u. and $L = 0 - 3$ and other parameters as in Figs. 5(a) and 5(b). Results are shown for seven values of R_0: 5 a.u. [dashed (red) lines], 10 a.u. [thick solid (black) lines], 15 a.u. [dash double-dotted (blue) lines], 20 a.u. [dashed (orange) lines], 25 a.u. [dashed (magenta) lines], 30 a.u. [dotted (green) lines], and 35 a.u. [thin solid (black) lines].

angular distributions produced by two attosecond pulses delayed in time by $\tau = \tau_{12}$ are shown in Fig. 6 for five projection times T_p: 20, 25, 35, 40, and 45 a.u. For $R_0 = 10$ a.u. and $L = 0 - 3$, it is clear that good convergence is reached for projection times $T_p \geqslant 25$ a.u. (i.e., 11–20 optical cycles after the end of pulses).

3. Dependence of the angular distributions on the outer radial boundary R_0 of bound and singly ionized states

To obtain the doubly ionized part, $\Psi_C(\mathbf{r}_1, \mathbf{r}_2; R, T_f + T_p)$, of the solution $\Psi(\mathbf{r}_1, \mathbf{r}_2; R, t)$ of the TDSE, we must remove contributions from both bound and singly ionized states. This is done by setting the wave packet $\Psi(\mathbf{r}_1, \mathbf{r}_2; R, t)$ equal to zero for radial distances $r_1 < R_0$ and/or $r_2 < R_0$, where R_0 defines the outer radial boundary of bound and singly ionized states [15,26]. The R_0 dependence of our TDSE results is shown in Fig. 7. For $T_p = 35$ a.u., we find that using a cutoff of $R_0 = 5$, 10, 15, or 20 a.u. leads to the same converged angular distributions. For larger values of R_0, e.g., $R_0 = 25$, 30, and 35 a.u., the TDSE results at $T_p = 35$ a.u. are unstable and decrease sharply. This behavior is expected because at that projection time T_p a significant contribution from the doubly ionized wave packet has been cut. In other words, the doubly ionized wave packet has not been given sufficient time to leave the region where either $r_1 < R_0$ or $r_2 < R_0$ [15]. All results presented in the main text have been obtained for $R_0 = 10$ a.u., which is the same value used in [15].

APPENDIX B: PERTURBATION THEORY ANALYSIS

We provide in this Appendix derivations of Eq. (4) for the transition amplitude for the two cases of chiral pulses propagating along $\hat{\mathbf{k}}$ either parallel ($\hat{\mathbf{k}} \parallel \mathbf{R}$) or perpendicular ($\hat{\mathbf{k}} \perp \mathbf{R}$) to the molecular axis $\mathbf{R}$. Also, we provide derivations of Eqs. (5) and (8) for the dynamical parameters of their DPI amplitudes, as well as of Eqs. (7) and (9) for their SDPs.

For convenience, we summarize first some notations applicable to all derivations. The expression for the effective polarization vector $\mathbf{e}'$ of the pulse pair is [8]

$$\mathbf{e}' = \mathbf{e} + e^{i\Phi}\mathbf{e}^*, \tag{B1}$$

where Φ is the Ramsey phase,

$$\Phi = (E + E_b)\tau + \phi_{12}, \tag{B2}$$

in which $E = (p_1^2 + p_2^2)/2$ is the energy of the electron pair in the continuum, E_b is the binding energy of the H_2 ground state, and $\phi_{12} = \phi_1 - \phi_2$ denotes the relative carrier-envelope phase (CEP) of the two pulses. In Eq. (B1), $\mathbf{e}$ is the first-pulse polarization vector:

$$\mathbf{e} = (\hat{\boldsymbol{\epsilon}} + i\eta\hat{\boldsymbol{\xi}})/(1 + \eta^2)^{1/2}, \tag{B3}$$

where $\eta \equiv \eta_1 = -\eta_2$ is its ellipticity, and $\hat{\boldsymbol{\epsilon}}$ and $\hat{\boldsymbol{\xi}} = (\hat{\mathbf{k}} \times \hat{\boldsymbol{\epsilon}})$ are the major and minor axes of the polarization ellipse, respectively. We define the x, y, and z axes of the laboratory frame respectively along $\hat{\boldsymbol{\epsilon}}$, $\hat{\boldsymbol{\xi}}$, and $\hat{\mathbf{k}}$. The linear and circular polarization degrees are, respectively:

$$\ell = (1 - \eta^2)/(1 + \eta^2), \tag{B4}$$

$$\xi = 2\eta/(1 + \eta^2). \tag{B5}$$

For later use, we note the following two relations:

$$1 + \ell = 2/(1 + \eta^2), \quad 1 - \ell = 2\eta^2/(1 + \eta^2). \tag{B6}$$

In the laboratory coordinate frame the scalar product of the effective polarization vector $\mathbf{e}'$ with an arbitrary vector $\mathbf{p} \equiv (p, \theta, \varphi)$ can be written as

$$(\mathbf{e}' \cdot \mathbf{p}) = e^{i\Phi/2}\frac{2p\sin\theta}{\sqrt{1+\eta^2}}[\cos\varphi\cos(\Phi/2) + \eta\sin\varphi\sin(\Phi/2)]. \tag{B7}$$

After some simple trigonometric transformations, Eq. (B7) can be expressed in terms of the circular polarization degree ξ [see Eq. (B5)] as

$$(\mathbf{e}' \cdot \mathbf{p}) = e^{i\Phi/2}p\sin\theta\{\sqrt{1+|\xi|}\cos(\Phi/2 - \hat{\xi}\varphi) + \sqrt{1-|\xi|}\cos(\Phi/2 + \hat{\xi}\varphi)\}, \tag{B8}$$

where $\hat{\xi} = \xi/|\xi| = \mathrm{sign}(\eta)$.

1. Amplitude and SDP for DPI of H_2 in the $\hat{\mathbf{k}} \parallel \mathbf{R}$ geometry

We derive here Eqs. (4), (5), and (7) of the main text for the detection geometry described by Figs. 1(a) and 1(b).

For $\hat{\mathbf{k}} \parallel \mathbf{R}$, $(\hat{\mathbf{R}} \cdot \mathbf{e}') = 0$ and the perturbation theory (PT) amplitude $\mathcal{A}$ given by Eq. (2) in the main text reduces to

$$\mathcal{A}_\parallel = e^{-i\phi_1}[A_{\Pi,1}(\chi)(\mathbf{e}' \cdot \hat{\mathbf{p}}_1) + A_{\Pi,2}(\chi)(\mathbf{e}' \cdot \hat{\mathbf{p}}_2)]. \tag{B9}$$

Here $A_{\Pi,1}(\chi)$ and $A_{\Pi,2}(\chi)$ are true scalar functions of $\chi \equiv (p_1, p_2, R, u, u_1, u_2)$, where p_1 and p_2 are the magnitudes of the electron momenta $\mathbf{p}_1$ and $\mathbf{p}_2$, $R = 1.4$ a.u. is the internuclear separation, $u \equiv (\hat{\mathbf{p}}_1 \cdot \hat{\mathbf{p}}_2)$, and $u_{1,2} \equiv (\hat{\mathbf{R}} \cdot \hat{\mathbf{p}}_{1,2})$. For the detection geometries in which either $\mathbf{p}_1 \parallel \hat{\mathbf{k}}$ and $\mathbf{p}_2$ is in the laser polarization plane [see Fig. 1(a) in the main text] or both electrons are emitted back-to-back (BTB) in the laser polarization plane [see Fig. 1(b) in the main text], the PT amplitude $\mathcal{A}_\parallel$ (B9) takes the form

$$\mathcal{A}_\parallel = e^{-i\phi_1}\, A_\Pi(\chi)(\mathbf{e}' \cdot \hat{\mathbf{p}}). \tag{B10}$$

In Eq. (B10), for the geometry in Fig. 1(a) in the main text, $\hat{\mathbf{p}} \equiv \hat{\mathbf{p}}_2$ and $A_\Pi(\chi) \equiv A_{\Pi,2}(\chi)$, where $\chi = (p_1, p_2, R, 0, 1, 0)$, whereas for the geometry in Fig. 1(b) in the main text, $\hat{\mathbf{p}} \equiv \hat{\mathbf{p}}_2 = -\hat{\mathbf{p}}_1$ and $A_\Pi(\chi) \equiv A_{\Pi,2}(\chi) - A_{\Pi,1}(\chi)$, where $\chi = (p_1, p_2, R, -1, 0, 0)$. Since the two electrons have zero total spin in the $^1\Sigma_g^+$ initial state, the coefficients $A_{\Pi,1}$ and $A_{\Pi,2}$ obey the symmetry relation,

$$A_{\Pi,1}(p_1, p_2, u_1, u_2) = A_{\Pi,2}(p_2, p_1, u_2, u_1), \quad \text{(B11)}$$

where for brevity we have omitted R and u from the list of arguments. From the symmetry property (B11), it follows that the PT amplitude $\mathcal{A}_\parallel$ (B10) vanishes for BTB emission of electrons with equal energy sharing since $A_{\Pi,1}(p_1, p_1, 0, 0) = A_{\Pi,2}(p_1, p_1, 0, 0)$.

Substituting the geometric factor $(\mathbf{e}' \cdot \mathbf{p})$ in Eq. (B8) into Eq. (B10), we obtain that the PT amplitude in spherical coordinates can be represented as a superposition of two vortex amplitudes with opposite handedness:

$$\mathcal{A}_\parallel = A_{\eta,\parallel}^{(+)} \cos(\Phi/2 - \hat{\xi}\varphi) + A_{\eta,\parallel}^{(-)} \cos(\Phi/2 + \hat{\xi}\varphi), \quad \text{(B12)}$$

which is Eq. (4) in the main text, where the dynamical parameters $A_{\eta,\parallel}^{(\pm)}$ are defined by

$$A_{\eta,\parallel}^{(\pm)} = e^{i(\Phi/2-\phi_1)} \sqrt{(1+\ell)/2} \sin\theta (1 \pm |\eta|) A_\Pi. \quad \text{(B13)}$$

For geometries in Figs. 1(a) and 1(b), $\theta = \pi/2$, and Eq. (B13) leads to Eq. (5) in the main text.

For circularly polarized pulses, $|\xi| = |\eta| = 1$ and the second term in Eq. (B12) vanishes. For elliptically polarized pulses, $|\xi| < 1$, Eq. (B12) has contributions from two kinematic vortex factors having opposite handedness, $\cos(\Phi/2 \pm \hat{\xi}\varphi)$. Taking the square modulus of Eq. (B12), the SDP, $\mathcal{W}_\parallel = |\mathcal{A}_\parallel|^2$, for two time-delayed counter-rotating chiral pulses with $\hat{\mathbf{k}} \parallel \mathbf{R}$ is

$$\begin{aligned}\mathcal{W}_\parallel = |A_\Pi(\chi)|^2 \sin^2\theta \{&(1+|\xi|)\cos^2(\Phi/2 - \hat{\xi}\varphi) \\ &+ (1-|\xi|)\cos^2(\Phi/2 + \hat{\xi}\varphi) \\ &+ 2\ell \cos(\Phi/2 - \hat{\xi}\varphi)\cos(\Phi/2 + \hat{\xi}\varphi)\}. \quad \text{(B14)}\end{aligned}$$

One sees that for small ℓ, one has $\xi \approx 1$, and the first vortex term dominates in the SDP (B14).

Alternatively, substituting the geometric factor $(\mathbf{e}' \cdot \mathbf{p})$ in Eq. (B7) in spherical coordinates into Eq. (B10) and using Eqs. (B4) and (B5), another expression for the SDP in the polarization plane ($\theta = \pi/2$) can be derived:

$$\begin{aligned}\mathcal{W}_\parallel = &\, 2(1-\ell)|A_\Pi(\chi)|^2 \sin^2\varphi \sin^2(\Phi/2) \\ &+ 2(1+\ell)\,|A_\Pi(\chi)|^2 \cos^2\varphi \cos^2(\Phi/2) \\ &+ \xi |A_\Pi(\chi)|^2 \sin(2\varphi)\sin\Phi. \quad \text{(B15)}\end{aligned}$$

For time-delayed counter-rotating circularly polarized pulses, $\ell = 0$ and $\xi = \pm 1$. Thus, the SDP in either Eq. (B14) or in Eq. (B15) reduces to

$$\mathcal{W}_\parallel = 2|A_\Pi(\chi)|^2 \sin^2\theta \cos^2(\Phi/2 - \xi\varphi), \quad \text{(B16)}$$

which is Eq. (7) in the main text.

2. Amplitude and SDP for DPI of H_2 in the $\hat{\mathbf{k}} \perp \mathbf{R}$ geometry

Below we show that the amplitude in the perpendicular geometry has the same form [see Eq. (4) in the main text] as in the parallel geometry, Eq. (B12). We also derive Eq. (8) for the dynamical parameters, as well as Eq. (9) for the SDP.

For $\hat{\mathbf{k}} \perp \mathbf{R}$, the PT amplitude (1) in the main text for the two detection geometries in Figs. 1(c) and 1(d) can be written, using Eq. (B1), as

$$\mathcal{A}_\perp = e^{-i\phi_1}[A_\Pi(\chi)(\mathbf{e}' \cdot \hat{\mathbf{p}}) + B(\chi)(\hat{\mathbf{R}} \cdot \mathbf{e}')(\hat{\mathbf{R}} \cdot \hat{\mathbf{p}})], \quad \text{(B17)}$$

where $B(\chi) \equiv A_\Sigma(\chi) - A_\Pi(\chi)$. Here, for the detection geometry in Fig. 1(c) in the main text, $\hat{\mathbf{p}} \equiv \hat{\mathbf{p}}_2$, $A_\Pi(\chi) \equiv A_{\Pi,2}(\chi)$, and $A_\Sigma(\chi) \equiv A_{\Sigma,2}(\chi)$, where $\chi = (p_1, p_2, R, 0, 0, \cos\varphi)$, whereas for the detection geometry in Fig. 1(d) in the main text, $\hat{\mathbf{p}} \equiv \hat{\mathbf{p}}_2 = -\hat{\mathbf{p}}_1$, $A_\Pi(\chi) \equiv A_{\Pi,2}(\chi) - A_{\Pi,1}(\chi)$, and $A_\Sigma(\chi) \equiv A_{\Sigma,2}(\chi) - A_{\Sigma,1}(\chi)$, where $\chi = (p_1, p_2, R, -1, -\cos\varphi, \cos\varphi)$. As the total spin for the two electrons is zero in the initial $^1\Sigma_g^+$ ground state, the coefficients $A_{\Pi,1}$ and $A_{\Pi,2}$ satisfy the symmetry relation (B11), and the coefficients $A_{\Sigma,1}$ and $A_{\Sigma,2}$ satisfy

$$A_{\Sigma,1}(p_1, p_2, u_1, u_2) = A_{\Sigma,2}(p_2, p_1, u_2, u_1), \quad \text{(B18)}$$

where for brevity we have omitted R and u from the list of arguments. From the symmetry properties (B11) and (B18), it follows that the PT amplitude $\mathcal{A}_\perp$ (B17) vanishes for BTB emission of electrons with EES. (This important result holds for any laser propagation direction $\hat{\mathbf{k}}$ and molecular orientation $\mathbf{R}$.)

For both detection geometries in Figs. 1(c) and 1(d) in the main text, $\hat{\mathbf{k}} \parallel \hat{\mathbf{z}}$, $\mathbf{R} \parallel \hat{\mathbf{x}}$, and $\mathbf{p} \equiv \mathbf{p}_2$ is detected in the polarization xy plane. The geometric factor $(\hat{\mathbf{R}} \cdot \mathbf{e}')$ in Eq. (B17) can be evaluated using Eq. (B7) by setting $p = 1$, $\theta = \pi/2$, and $\varphi = 0$; one then obtains

$$(\hat{\mathbf{R}} \cdot \mathbf{e}') = e^{i\Phi/2}[2/(1+\eta^2)^{1/2}]\cos(\Phi/2). \quad \text{(B19)}$$

Using this equation and noting that $(\hat{\mathbf{R}} \cdot \hat{\mathbf{p}}) = \sin\theta\cos\varphi$, Eq. (B17) for the amplitude becomes

$$\mathcal{A}_\perp = e^{i(\Phi/2-\phi_1)}[\sin\theta/(1+\eta^2)^{1/2}]\tilde{A}_\perp, \quad \text{(B20)}$$

where $\tilde{\mathcal{A}}_\perp$ is defined by

$$\begin{aligned}\tilde{\mathcal{A}}_\perp &= 2[A_\Sigma \cos\varphi \cos(\Phi/2) + \eta A_\Pi \sin\varphi \sin(\Phi/2)] \\ &= (A_\Sigma + |\eta| A_\Pi)\cos(\Phi/2 - \hat{\xi}\varphi) \\ &\quad + (A_\Sigma - |\eta| A_\Pi)\cos(\Phi/2 + \hat{\xi}\varphi). \quad \text{(B21)}\end{aligned}$$

As a result, Eq. (B20) can be written in the compact form [which is Eq. (4) in the main text]:

$$\mathcal{A}_\perp = A_{\eta,\perp}^{(+)} \cos(\Phi/2 - \hat{\xi}\varphi) + A_{\eta,\perp}^{(-)} \cos(\Phi/2 + \hat{\xi}\varphi), \quad \text{(B22)}$$

where the dynamical parameters $A_{\eta,\perp}^{(\pm)}$ are defined by

$$A_{\eta,\perp}^{(\pm)} = e^{i(\Phi/2-\phi_1)} \sqrt{(1+\ell)/2} \sin\theta [A_\Sigma \pm |\eta| A_\Pi]. \quad \text{(B23)}$$

For $\theta = \pi/2$, Eq. (B23) reduces to Eq. (8) in the main text. Taking the square modulus of $\mathcal{A}_\perp$ in Eq. (B20) or in Eq. (B22) in the laser polarization xy plane ($\theta = \pi/2$), and using the relations (B6), one obtains

$$\begin{aligned}\mathcal{W}_\perp = &\, 2(1-\ell)|A_\Pi(\chi)|^2 \sin^2\varphi \sin^2(\Phi/2) \\ &+ 2(1+\ell)\,|A_\Sigma(\chi)|^2 \cos^2\varphi \cos^2(\Phi/2) \\ &+ \xi\, \mathrm{Re}\,[A_\Sigma^*(\chi) A_\Pi(\chi)] \sin(2\varphi)\sin\Phi, \quad \text{(B24)}\end{aligned}$$

which is Eq. (9) in the main text.

[1] N. F. Ramsey, A molecular beam resonance method with separated oscillating fields, Phys. Rev. **78**, 695 (1950).

[2] J. M. N. Djiokap, S. X. Hu, L. B. Madsen, N. L. Manakov, A. V. Meremianin, and A. F. Starace, Electron Vortices in Photoionization by Circularly Polarized Attosecond Pulses, Phys. Rev. Lett. **115**, 113004 (2015).

[3] J. M. N. Djiokap, A. V. Meremianin, N. L. Manakov, S. X. Hu, L. B. Madsen, and A. F. Starace, Multistart spiral electron vortices in ionization by circularly polarized UV pulses, Phys. Rev. A **94**, 013408 (2016).

[4] D. Pengel, S. Kerbstadt, D. Johannmeyer, L. Englert, T. Bayer, and M. Wollenhaupt, Electron Vortices in Femtosecond Multiphoton Ionization, Phys. Rev. Lett. **118**, 053003 (2017).

[5] D. Pengel, S. Kerbstadt, L. Englert, T. Bayer, and M. Wollenhaupt, Control of three-dimensional electron vortices from femtosecond multiphoton ionization, Phys. Rev. A **96**, 043426 (2017).

[6] K.-J. Yuan, S. Chelkowski, and A. D. Bandrauk, Photoelectron momentum distributions of molecules in bichromatic circularly polarized attosecond UV laser fields, Phys. Rev. A **93**, 053425 (2016).

[7] K.-J. Yuan, H. Lu, and A. D. Bandrauk, Photoionization of triatomic molecular ions H_3^{2+} by intense bichromatic circularly polarized attosecond UV laser pulses, J. Phys. B **50**, 124004 (2017).

[8] J. M. N. Djiokap, A. V. Meremianin, N. L. Manakov, S. X. Hu, L. B. Madsen, and A. F. Starace, Kinematical vortices in double photoionization of helium by attosecond pulses, Phys. Rev. A. **96**, 013405 (2017).

[9] J. M. N. Djiokap and A. F. Starace, Doubly-excited state effects on two-photon double ionization of helium by time-delayed, oppositely circularly-polarized attosecond pulses, J. Opt. **19**, 124003 (2017).

[10] Z. L. Li, Y. J. Li, and B. S. Xie, Momentum vortices on pairs production by two counter-rotating fields, Phys. Rev. D **96**, 076010 (2017).

[11] M. Li, G. Zhang, T. Zhao, X. Ding, and J. Yao, Electron vortices in photoionization by a pair of elliptically polarized attosecond pulses, Chin. Opt. Lett. **15**, 120202 (2017).

[12] M. Li, G. Zhang, X. Kong, T. Wang, X. Ding, and J. Yao, Dynamic Stark induced vortex momentum of hydrogen in circular fields, Opt. Express **26**, 878 (2018).

[13] X. Kong, G. Zhang, M. Li, T. Wang, X. Ding, and J. Yao, Odd-fold-symmetric spiral momentum distributions and their Stark distortions in hydrogen, J. Opt. Soc. Am. B **35**, 2163 (2018).

[14] J. Colgan, M. S. Pindzola, and F. Robicheaux, Triple Differential Cross Sections for the Double Photoionization of H_2, Phys. Rev. Lett. **98**, 153001 (2007).

[15] I. A. Ivanov and A. S. Kheifets, Time-dependent calculations of double photoionization of the aligned H_2 molecule, Phys. Rev. A **85**, 013406 (2012).

[16] W. Vanroose, F. Martín, T. N. Rescigno, and C. W. McCurdy, Complete photo-induced breakup of the H_2 molecule as a probe of molecular electron correlation, Science **310**, 1787 (2005).

[17] W. Vanroose, D. A. Horner, F. Martín, T. N. Rescigno, and C. W. McCurdy, Double photoionization of aligned molecular hydrogen, Phys. Rev. A **74**, 052702 (2006).

[18] L. Tao, C. W. McCurdy, and T. N. Rescigno, Grid-based methods for diatomic quantum scattering problems, III. Double photoionization of molecular hydrogen in prolate spheroidal coordinates, Phys. Rev. A **82**, 023423 (2010).

[19] X. Guan, K. Bartschat, and B. I. Schneider, Breakup of the aligned H_2 molecule by XUV laser pulses: A time-dependent treatment in prolate spheroidal coordinates, Phys. Rev. A **83**, 043403 (2011).

[20] W.-C. Jiang, L.-Y. Peng, J.-W. Geng, and Q. Gong, One-photon double ionization of H_2 with arbitrary orientation, Phys. Rev. A **88**, 063408 (2013).

[21] J. M. N. Djiokap, N. L. Manakov, A. V. Meremianin, S. X. Hu, L. B. Madsen, and A. F. Starace, Nonlinear Dichroism in Back-to-Back Double Ionization of He by an Intense Elliptically Polarized Few-Cycle Extreme Ultraviolet Pulse, Phys. Rev. Lett. **113**, 223002 (2014).

[22] C. W. McCurdy, M. Baertschy, and T. N. Rescigno, Solving the three-body Coulomb breakup problem using exterior complex scaling, J. Phys. B **37**, R137 (2004).

[23] S. X. Hu, Optimizing the FEDVR-TDCC code for exploring the quantum dynamics of two-electron systems in intense laser pulses, Phys. Rev. E **81**, 056705 (2010).

[24] H. G. Muller, An efficient propagation scheme for the time-dependent Schrödinger equation in the velocity gauge, Laser Physics **9**, 138 (1999).

[25] T. K. Kjeldsen, L. A. A. Nikolopoulos, and L. B. Madsen Solving the m-mixing problem for the three-dimensional time-dependent Schrödinger equation by rotations: Application to strong-field ionization of H_2^+, Phys. Rev. A **75**, 063427 (2007).

[26] L. B. Madsen, L. A. A. Nikolopoulos, T. K. Kjeldsen, and J. Fernández, Extracting continuum information from $\Psi(t)$ in time-dependent wave-packet calculations, Phys. Rev. A **76**, 063407 (2007).

[27] J. M. Feagin, A helium-like description of molecular hydrogen photo-double ionization, J. Phys. B **31**, L729 (1998).

[28] D. A. Horner, W. Vanroose, T. N. Rescigno, F. Martín, and C. W. McCurdy, Role of Nuclear Motion in Double Ionization of Molecular Hydrogen by a Single Photon, Phys. Rev. Lett. **98**, 073001 (2007).

[29] T. J. Reddish, J. Colgan, P. Bolognesi, L. Avaldi, M. Gisselbrecht, M. Lavollée, M. S. Pindzola, and A. Huetz, Physical Interpretation of the "Kinetic Energy Release" Effect in the Double Photoionization of H_2, Phys. Rev. Lett. **100**, 193001 (2008).

[30] D. A. Horner, S. Miyabe, T. N. Rescigno, C. W. McCurdy, F. Morales, and F. Martín, Classical Two-Slit Interference Effects in Double Photoionization of Molecular Hydrogen at High Energies, Phys. Rev. Lett. **101**, 183002 (2008).

[31] See Supplemental Material at http://link.aps.org/supplemental/10.1103/PhysRevA.98.063407 for an animation of the evolution of the dynamical vortex patterns with ellipticity η over the range $0.001 \leqslant \eta \leqslant 1$ for the BTB UES detection geometry in Fig. 1(d) and for the same laser parameters as in Fig. 3(c). In the animation, seven values of the ellipticity η are employed in this range: $\eta(0) \equiv 1$, $\eta(1) \equiv 0.5$, $\eta(2) \equiv 0.4$, $\eta(3) \equiv 0.3$, $\eta(4) \equiv 0.2$, $\eta(5) \equiv 0.05$, and $\eta(6) \equiv 0.001$. Note that dynamical vortices appear only for five values of $\eta(j)$, where $1 \leqslant j \leqslant 5$.

[32] T. E. Sharp, Potential-energy curves for molecular hydrogen and its ions, Atomic Data **2**, 119 (1971).

[33] J. S. Sims and S. A. Hagstrom, High precision variational calculations for the Born-Oppenheimer energies of the ground state of the hydrogen molecule, J. Chem. Phys. **124**, 094101 (2006).